Controlled meteorological (CMET) balloon profiling of the Arctic atmospheric boundary layer around Spitsbergen compared to a mesoscale model

Tjarda J Roberts, P. B. Voss, M. Dütsch, L. R. Hole

Atmos. Chem. Phys. Discuss., 15, 27539–27573, 2015
www.atmos-chem-phys-discuss.net/15/27539/2015/
doi:10.5194/acpd-15-27539-2015

Atmospheric Chemistry and Physics Discussions

Controlled meteorological (CMET) balloon profiling of the Arctic atmospheric boundary layer around Spitsbergen compared to a mesoscale model

T. J. Roberts[1,2], **M. Dütsch**[3,4], **L. R. Hole**[3], **and P. B. Voss**[5]

[1]LPC2E/CNRS, 3A, Avenue de la Recherche Scientifique, 45071 Orléans, CEDEX 2, France
[2]Norwegian Polar Institute, Fram Centre, 9296 Tromsø, Norway
[3]Norwegian Meteorological Institute, Bergen, Norway
[4]ETH Zürich, Switzerland
[5]Smith College, Picker Engineering Program, Northampton MA, USA

Received: 22 May 2015 – Accepted: 12 September 2015 – Published: 14 October 2015

Correspondence to: T. J. Roberts (tjardaroberts@gmail.com)

Published by Copernicus Publications on behalf of the European Geosciences Union.

Abstract

Observations from CMET (Controlled Meteorological) balloons are analyzed in combination with mesoscale model simulations to provide insights into tropospheric meteorological conditions (temperature, humidity, wind-speed) around Svalbard, European High Arctic. Five Controlled Meteorological (CMET) balloons were launched from Ny-Ålesund in Svalbard over 5–12 May 2011, and measured vertical atmospheric profiles above Spitsbergen Island and over coastal areas to both the east and west. One notable CMET flight achieved a suite of 18 continuous soundings that probed the Arctic marine boundary layer over a period of more than 10 h. The CMET profiles are compared to simulations using the Weather Research and Forecasting (WRF) model using nested grids and three different boundary layer schemes. Variability between the three model schemes was typically smaller than the discrepancies between the model runs and the observations. Over Spitsbergen, the CMET flights identified temperature inversions and low-level jets (LLJ) that were not captured by the model. Nevertheless, the model largely reproduced time-series obtained from the Ny-Ålesund meteorological station, with exception of surface winds during the LLJ. Over sea-ice east of Svalbard the model underestimated potential temperature and overestimated wind-speed compared to the CMET observations. This is most likely due to the full sea-ice coverage assumed by the model, and consequent underestimation of ocean–atmosphere exchange in the presence of leads or fractional coverage. The suite of continuous CMET soundings over a sea-ice free region to the northwest of Svalbard are analysed spatially and temporally, and compared to the model. The observed along-flight daytime increase in relative humidity is interpreted in terms of the diurnal cycle, and in the context of marine and terrestrial air-mass influences. Analysis of the balloon trajectory during the CMET soundings identifies strong wind-shear, with a low-level channeled flow. The study highlights the challenges of modelling the Arctic atmosphere, especially in coastal zones with varying topography, sea-ice and surface conditions. In this context, CMET balloons provide a valuable technology for profiling the free atmosphere

ACPD
15, 27539–27573, 2015

and boundary layer in remote regions where few other observations are available for model validation.

1 Introduction

The polar regions provide a challenge to atmospheric numerical models. Firstly, model parameterisations are often adapted to and validated against lower latitudes and might not necessarily be applicable to high latitude processes. Secondly, there exists limited detailed in-situ observational data for model initialization and validation in remote polar regions. Accurate representation polar meteorology and small-scale processes, is, however, essential for meteorological forecast models, whose comparison to observations is particularly relevant for improving understanding of climate in the Arctic, a region undergoing rapid change (Vihma, 2014). A particular challenge is that the polar atmospheric boundary layer (ABL) is usually strongly stable during winter, and only weakly stable to neutral during summer (Persson et al., 2002). This stability acts to magnify the effects of flows over small scale topography, such as channeling, katabatic flows and mountain waves, and can promote the formation of low-level jets. Further, in coastal areas, thermodynamic ice formation, growth and melt, and wind- and oceanic current driven advection of sea ice can lead to highly variable surface conditions that control air–sea exchange of heat and momentum, and affect the radiative balance e.g. through albedo. Snow layers deposited upon sea-ice provide a further insulating layer that modifies heat exchange between the ocean and the overlying atmosphere. For example, for polar winter conditions at low atmospheric temperature (e.g. −40 °C), the surface temperature of open water areas is practically at the freezing point of water (−1.8 °C), while the surface temperature of thick snow covered sea ice is substantially lower, being close to the atmospheric temperature (e.g. −40 °C). Hence, the heat and energy fluxes can vary by up to two orders of magnitude, depending on the surface state (Kilpeläinen et al., 2011).

ACPD
15, 27539–27573, 2015

Thus, significant uncertainties remain in modelling Arctic meteorological variables. For example, a comparison of eight different RCM (Regional Climate Model) simulations over the Western Arctic to European Center for Medium–Range Weather Forecast (ECMWF) analyses over September 1997–September 1998 found general agreement to the model ensemble mean but large across-model variability, particularly in the lowest model levels (Rinke et al., 2006). Direct comparisons of Arctic ABL meteorology observations to mesoscale model simulations using the regional Weather Research and Forecasting (WRF) model (in standard or "polar" version) have also been performed. These include comparison to automatic weather stations (AWS) on the Greenland ice sheet in June 2001 and December 2002 (Hines and Bromwich, 2008); to drifting ice station SHEBA meteorological measurements over the Arctic Ocean in 1997–1998 (Bromwich et al., 2009); to tower observations and radio-sonde soundings in three Svalbard (Spistbergen) fjords in winter and spring 2008 (Kilpeläinen et al., 2011); to AWS stations along Kongsfjorden in Svalbard in spring 2010 (Livik, 2011); to meteorological mast measurements in Wahlenbergfjorden, Svalbard in May 2006 and April 2007 (Makiranta et al., 2011); to tethered balloon soundings and mast observations in Advent- and Kongsfjorden in Svalbard in March-April 2009 (Kilpeläinen et al., 2012), and to a remotely controlled model aircraft equipped with meteorological sensors (the small unmanned meteorological observer, SUMO) over Iceland and Advent valley in Svalbard (Mayer et al., 2012a, b). These studies collectively found that (Polar) WRF was able to partially reproduce the meteorological observations, typically only when operated at higher model resolution (e.g. 1 km). Sea-ice was found to be particularly important at high sea–air temperature differences, and occurrence of low-level jets were observed yet not always reproduced by the model. Such comparisons between model and observations are, however, limited by the spatial scale of the field observations, typically only a few km.

To provide an in-situ meteorological ABL dataset covering a wider Arctic region, we deployed five Controlled METteorological (CMET) balloons, launched in May 2011 from Ny-Ålesund on Svalbard. CMET balloons are capable of performing sustained flights

ACPD
15, 27539–27573, 2015

within the troposphere at designated altitudes, and can take vertical soundings at any time during the balloon flight on commanded via satellite link (Voss et al., 2013). The CMETs can also be configured for automated profiling of the atmospheric boundary layer during the flight, as we demonstrate in this study. The nested dual balloon design ensures very little helium loss, enabling the balloons to make multi-day flights. This gives the opportunity to investigate areas far away from research bases, at greater spatial scales (many hundreds of kilometers from the launch point) than can be obtained by line-of-sight unmanned aerial vehicle (UAV) approaches, radio-sondes or tethered balloons. Previous CMET balloon applications include Riddle et al. (2006), Voss et al. (2010), Mentzoni (2011) and Stenmark et al. (2014). Voss et al. (2010) investigated the evolving vertical structure of the polluted Mexico City Area outflow by making repeated balloon profile measurements of temperature, humidity and wind in the advecting outflow. Riddle et al. (2006) and Mentzoni (2011) used the CMET balloons as a tool to verify atmospheric trajectory models – namely FlexTra (Stohl et al., 1995) and FlexPart (Stohl et al., 1998) – in the United States and in the Arctic, respectively. Stenmark et al. (2014) combined data from CMETs, ground-based and a small model airplane data with WRF simulations to highlight the role of nunatak-induced convection in Antarctica.

Here we compare the soundings performed during the five Svalbard balloon flights of May 2011 to simulations made using the Weather Research and Forecasting (WRF) mesoscale model with three different boundary layer schemes, and thereby provide insights into key processes influencing meteorology of remote Arctic regions.

2 Methods

2.1 Observations

Five CMET balloons were launched from the research station of the Alfred Wegener Institute and the Polar Institute Paul Emile Victor (AWIPEV) in Ny Ålesund, over the

ACPD
15, 27539–27573, 2015

period 5 to 12 May 2011. The CMET payload included meteorological sensors for temperature, relative humidity (RH) and pressure, as well as GPS and satellite modem for in-flight control. The CMET balloon design and control algorithms are described in detail by Voss et al. (2013). Figure 1a and b shows the balloon flights of the May 2011 campaign as well as two meteorological sites providing additional ground-based data: the Ny-Ålesund AWI-PEV station (from where the balloons were launched), and Verlegenhuken in North-East Spitzbergen. Balloons 1 and 2 had short flights due to technical issues encountered at the start of the campaign, and included only one vertical sounding each. Balloon 3 flew far north but did not perform soundings after leaving the coastal area of Spitzbergen, thus only the vertical sounding (ascent and descent) at the very beginning of the flight is used for this study. Balloon 4 flew eastwards, but despite strong balloon performance needed to be terminated before encroaching Russian airspace. In addition to its vertical sounding obtained shortly after launch it includes two closely spaced (ascent and descent) soundings over sea-ice east of Svalbard. Balloon 5 undertook a 24 h duration flight that first exited Kongsfjorden, then flew northwards along the coast and measured a much longer series of 18 consecutive profiles of the ABL in automatic sounding mode, before being raised to higher altitudes where winds advected it eastwards (Voss et al., 2013). To the best of our knowledge, this was the first automated sounding sequence made by a free balloon.

Temperature and humidity profiles were extracted from the CMET flights for model comparison as indicated in Fig. 1a and b, in locations over Svalbard topography, over a sea-ice covered region east of Svalbard, and over a sea-ice free region west of Svalbard where continuous automated soundings were performed. The capacitance humidity sensor (G-TUCN.34 from UPSI, covering 2 to 98 % RH range over −40 to +85 °C) generates a signal which is a function of the ambient relative humidity (RH) with respect to water. Humidity was therefore reported as RH over (supercooled liquid) water, which is standard procedure for atmospheric balloon-sonde measurements (even at sub-zero temperatures). Land- and/or sea-ice were, however, present for some of the campaign locations (although not during the automated soundings of flight 5 over ice-

ACPD
15, 27539–27573, 2015

free ocean west of Svalbard). Where present, they could promote ice deposition, thus act to lower the water saturation vapour pressure. In such conditions, RH calculated over water underestimates the RH with respect to ice. Nevertheless, for the relatively warm ambient surface temperatures encountered over ice during the campaign (typically a few degrees negative °C or higher) such effects are modest. For consistency, RH over water is reported across the field-campaign and is similarly illustrated for the model output.

For comparison to two WRF nested model runs (see details below), the balloon profiles were interpolated to 50 m height intervals and the measurement from paired ascent/descent soundings were averaged at each height. These ascent/descent profiles typically each required between 30 min and about one hour depending on the altitude change. These averaged ascent/descent profiles were compared to WRF model output at the longitude and latitude of the balloon location at the maximum of its ascent/descent cycle, averaged over a full hour centred on the middle of the balloon profile. A more detailed analysis was made of the meteorological evolution observed during consecutive automated soundings of flight 5, by comparing to WRF output at selected times along a transect line approximately following the CMET flight path, and geographically within the model layer corresponding to the average CMET flight altitude.

2.2 Numerical model implementation

Regional model simulations were performed using the Weather Research and Forecast (WRF) version 3.3.1. It is based on non-hydrostatic and fully compressible Euler equations that are integrated along terrain-following hydrostatic-pressure (sigma) coordinates, see Skamarock et al. (2008). The model was run for the simulation period from 3 May 2011, 00:00 UTC to 12 May 2011, 00:00 UTC allowing for a spin up time of 48 h. An adaptive time-step was used (minimum 1 s) to avoid numerical instabilities. Three domains with a respective horizontal resolution of 9, 3 and 1 km were used, where the two inner domains both were two-way nested to their mother domain. The domain loca-

ACPD
15, 27539–27573, 2015

tions are shown in Fig. 2. The outer domain was centered at 78.9° N, 16.5° E (78.9° N, 19.5° E for model run 2) and included 114 × 94 gridpoints covering the whole Svalbard archipelago and a large part of the surrounding Arctic ocean. The second domain included 175 × 184 (187 × 202) gridpoints for model run 1 (model run 2) and covered the whole Svalbard archipelago, whilst the innermost domain, which covered the area where the correspondent balloon profiles and timeseries were measured, had 232 × 190 (253 × 202) gridpoints for model run 1 (model run 2). All three domains had a high vertical resolution with 61 terrain-following sigma levels, where the model top was set to 50 hPa. The lowest 1000 m included 19 model levels with the lowest full model level at 19 m. Static field data, such as topography and land use index, were provided by the US Geological Survey in a horizontal resolution of 30 arcseconds (0.9 km in north–south direction). Initial and lateral boundary conditions were taken from the ECMWF operational analysis data on a 0.125° × 0.125° horizontal resolution and on 91 vertical levels, and updated every six hours. Sea ice and sea surface temperature (SST) were taken directly from the ECMWF data at the time the simulation started (3 May 2011) and remained fixed during the whole simulation period, assuming full sea-ice coverage for any model grid-point with positive sea-ice flag. This approach is justified by the good agreement between the ECMWF sea-ice flag and satellite images of sea-ice coverage on 5 May, both showing dense sea-ice east of Svalbard (Fig. 3). Conversely, to the west of Svalbard, sea-ice is absent. Sea surface temperatures are, as usual, higher to the west than east of Svalbard. This is due to the northward flowing warm and saline Atlantic Warm Current (AWC) or "Gulf stream" that elevates temperatures along Svalbard's west coast (the AWC subsequently sinks below the cold polar waters further north).

For cloud microphysics the WRF single moment 3-class simple ice scheme (Dudhia, 1989; Hong et al., 2004) was used. Radiation was parameterised with the Rapid Radiative Transfer Model (RRTM) longwave scheme (Mlawer et al., 1997), and the Dudhia shortwave scheme (Dudhia, 1989). Surface fluxes were provided by the Noah Land Surface Model (LSM), a four-layer soil temperature and moisture model with snow

ACPD
15, 27539–27573, 2015

cover prediction (Chen and Dudhia, 2001). In the first and second domain, the Kain–Fritsch cumulus scheme (Kain, 2004) was applied in addition, whereas in the third domain, cumulus convection was neglected.

Sensitivity tests were made with three different boundary layer parameterisation schemes as follows: the Yonsei University (YSU) scheme (Hong et al., 2006) is a non-local first order closure scheme that uses a counter gradient term in the eddy diffusion equation, and is the default ABL scheme in WRF. The Mellor–Yamada–Janjic (MYJ) scheme (Janjic, 1990, 1996, 2002) uses the local 1.5 order (level 2.5) closure Mellor–Yamada model (Mellor and Yamada, 1982), where the eddy diffusion coefficient is determined from the prognostically calculated turbulent kinetic energy (TKE). According to Mellor and Yamada (1982), it is an appropriate scheme for stable to slightly unstable flows, while errors might occur in the free convection limit. The Quasi-Normal Scale Elimination (QNSE) scheme (Sukoriansky et al., 2006) is, as the MYJ scheme, a local 1.5 order closure scheme. In contrast to the MYJ scheme, it includes scale dependence by using only partial averaging instead of scale independent Reynolds averaging, and is therefore able to take into account the spatial anisotropy of turbulent flows. It is thus considered especially suited for the stable ABL.

3 Results and discussion

3.1 Meteorological conditions and ground-stations compared to the WRF simulation

The period of 3–12 May 2011 was characterized by rapidly changing meteorological conditions, reflected in the different CMET flight paths (Fig. 1a and b) and the 6 hourly averaged meteorological station surface observations shown in Fig. 4 (AWIPEV, Ny-Ålesund) and Supplement S1 (Verlegenhuken, N Svalbard). At first, northerly winds carried cold air to Ny-Ålesund, causing surface temperatures to decline, reaching an hourly minimum of −9.4 °C on 5 May. The wind direction then changed to southerly

ACPD
15, 27539–27573, 2015

winds over not much more than one day, leading to increasing temperatures and an hourly maximum of 2.9 °C on 6 May. The wind direction subsequently become more westerly and then northerly with high wind-speeds on 8 and 9 May, given occurrence of a high pressure system SW and a lower pressure system NE of Svalbard, and the AVIPEV station registered a maximum wind-speed of 17.4 $m\,s^{-1}$ around noon on 9 May. This was followed by a period of lowwind-speed over 11–12 May, also reflected in the 24 h CMET flight to the east of Svalbard, with low temperatures recorded at the Spitsbergen meteorological stations. The WRF simulations show good general agreement to the 6 hourly averaged surface meteorological observations at Ny-Ålesund, Fig. 4, (and Verlegenhuken station in N Svalbard, Fig. S1 in the Supplement), with similar results for all three ABL schemes. However, the high (> 10 $m\,s^{-1}$) southerly surface winds predicted on 6–7 May for Ny-Ålesund were not observed. Outside of these dates, the model generally reproduced the winds, albeit at a wind direction 30° greater (clockwise) than typically observed in Ny-Ålesund (see wind-roses, Fig. S2), likely due to a wind channeling effect in the Kongsfjorden that is not fully captured by the model. Temperature was well reproduced however somewhat overestimated during cold periods (e.g. 5 and 11–12 May) at both surface stations.

3.2 Atmospheric boundary layer over Spitsbergen: topography, inversions and low level jets

The four CMET soundings over Svalbard topography are compared to WRF wind-speed, relative humidity and temperature profiles in Fig. 5, for the three different boundary layer schemes. Notably the results using the three ABL schemes are not strongly differing from each other, but collectively show greater disagreement to the observed ABL profiles. WRF captures the profiles with weak winds (profile 1, 4) well, but not on 5–6 May (profile 2, 3) where the CMET observations show the occurrence of a weak low level jet (LLJ) with a wind-speed maximum at around 1200 m and lower wind-speeds above and below. WRF in contrast predicts the highest wind-speeds below 1000 m and also does not capture the observed inversion above 1300 m. Thus, the model difficulty

ACPD
15, 27539–27573, 2015

to predict the lofted altitude of the LLJ appears connected to the model overestimation of surface wind-speed in Ny-Ålesund on 5–6 May (a model-observation discrepancy not found in Verlegenhuken further north in Svalbard). The occurrence of LLJs is likely promoted by the Svalbard topography in conjunction with a stable boundary layer.

These model-observation discrepancies are consistent with previous studies: Molders and Kramm (2010) found that WRF had difficulties in capturing the full strength of the surface temperature inversion observed during a five day cold weather period in Alaska. Kilpeläinen et al. (2012) found that WRF reproduced only half the observed inversions, and often underestimated their depth and strength, and that the average modeled LLJ was deeper and stronger than that observed. An overestimation of surface wind-speeds by WRF, especially in case of strong winds, has also been reported by Claremar et al. (2012), in comparison to AWS placed on three Svalbard glaciers, and by Kilpeläinen et al. (2011) and Kilpeläinen et al. (2012), in a study of Kongsfjorden. Since low wind-speeds are associated with inversion formation, WRF's overestimation of wind-speed might partly explain the difficulties in capturing (the strength of) inversions (Molders and Kramm, 2010). Consequently, since elevated inversions are often connected to low level jets (Andreas et al., 2000), the difficulties in capturing inversions could help explain the model difficulties in predicting low level jets.

A likely limitation to the WRF model capability over complex topography is its horizontal and vertical resolution. The model set-up used here includes 61 vertical layers, which Mayer et al. (2012b) suggests are necessary to resolve ABL phenomena, such as low level jets. However, Esau and Repina (2012) note that even a model resolution of 1 km in the horizontal does not properly represent the valley and steep surrounding mountains in Kongsfjorden, finding that even a fine resolution model (56×61 m grid cell, 20 times higher than the 1 km grid cell used in this and other WRF studies) could not fully resolve near-surface small-scale turbulence in the strongly stratified Kongsfjorden atmosphere.

ACPD
15, 27539–27573, 2015

3.3 CMET atmospheric profiles east of Spitsbergen: the role of sea-ice

The two consecutive CMET profiles over sea-ice east of Svalbard are compared to WRF model run 2 in Fig. 6. All three schemes tend to overestimate wind-speed, especially at the low levels. Nevertheless the slope of the wind profile corresponds approximately to the observations. Potential temperature is underestimated by around 2.5 K in all schemes. The largest difference between the observations and the model is found at the low levels, where it reaches up to 4 K. However, relative humidity is in better agreement, meaning that specific humidity must also be lower in the model than in the observations (e.g. a 4 K difference at 85 % RH corresponds to a 9×10^{-4} kg m^{-3} absolute humidity, a difference of around one quarter to one third ambient levels). The temperature and specific humidity bias is most probably due to an over representation of sea ice in the WRF model setup, which exerts a strong control on surface conditions. Even though the sea ice flag from the ECMWF data seems to agree fairly well with satellite sea-ice observations (Fig. 3), areas of polynyas and leads that can be recognized on the satellite picture were represented as homogeneous sea ice in the model. Further, the 100 % sea-ice coverage assumed in the model for grid cells with positive sea-ice flag may not reflect reality: small patches of open water amongst very close (90–100 %) or close (80–90 %) drift ice would promote sea–air exchange, enhancing both temperature and specific humidity at the surface (Andreas et al., 2002).

Inclusion of fractional sea-ice in WRF (available for WRF version 3.1.1 and higher) might rectify this problem, but is not straightforward to implement: the amount of sea ice in a grid cell varies with time through sea ice formation, break up and drifting, the latter typically a dominant control on ice-presence during late spring east of Svalbard. However, the WRF meteorological model does not simulate surface oceanographic processes, thus predicted sea-ice presence depended only on whether the SST was above or below the freezing point of sea-water. An option is to remove excessive sea ice manually, as, e.g., in Mayer et al. (2012b) or to update the sea ice field and the SST at certain intervals (e.g. six hours) with data from observations or re-analyses,

ACPD
15, 27539–27573, 2015

as in Kilpeläinen et al. (2012), but this becomes demanding over large regions. Nevertheless, given its strong control on ABL processes, a fractional sea-ice approach is recommended for future studies, particularly if a longer series of CMET soundings can be achieved, e.g. during balloon flights advected in a pole-ward direction, rather than towards Russia, which necessitated the flight to be terminated on command after only two profiles in our study.

3.4 Automated CMET soundings during a 24 h flight west of Spitsbergen

Flight 5 provided a series of 18 boundary-layer profiles over a largely sea-ice free region west of Svalbard. With the low wind-speeds ($< 5\,m\,s^{-1}$), the 24 h balloon trajectory remained relatively close to Svalbard coastline. Figure 7 shows the observed profiles of potential temperature, specific humidity, wind-speed and wind-direction, with interpolated data between the soundings. The soundings ranged from approximately 150 to 700 m during the first part of the flight (~ 02:00–12:30 UTC, JD 131.08–131.52). Specific humidity is greatest and potential temperature lowest nearer the surface, as expected. Specific humidity tends to increase during the flight, particularly in the lower and middle levels, which can be interpreted as a diurnal enhancement from surface evaporation. However, beyond JD 131.40 (09:36 UTC) there is actually a decrease in humidity in the lowermost levels, with maximum humidity in the sounding occurring around 350 m. Concurrent to this there is also a small increase in potential temperature at low altitudes. The wind-speed and direction plots indicate relatively calm conditions, with greatest wind-speed in the lower levels generally from a southerly direction. In contrast, at the top of the soundings the balloon encountered winds from a northerly direction, above 600 m. From JD 131.35 onwards, the observed winds became broadly southerly also at 600 m. However, a band of rather more west-south-westerly winds developed at mid-altitudes (~ 450 m), and low-level winds became (east)-south-easterly from JD 131.4 onwards. An important overall conclusion from these measurements is that the balloon was not sampling a uniform air-mass during this flight, rather it encountered a variety of air mass properties and behaviours over the course of the soundings.

ACPD
15, 27539–27573, 2015

While the complex flow in this case largely precludes a quasi-Lagrangian-type process study, the series of profiles none-the-less provides a nuanced understanding that is not possible with traditional rawinsondes or constant-altitude balloons.

The CMET observations appear consistent with the occurrence of a low-level flow that is decoupled from higher altitudes, and – at least initially – a diurnal increase in surface humidity through enhanced ocean evaporation. The observed wind-shear is consistent with a tilted high pressure system (that tilts with altitude towards the west of Svalbard, according to the WRF model), whilst surface winds may be further influenced by low-level channel flows. An outflow commonly exits from nearby Kongsfjorden-Kongsvegen valley (e.g. Esau and Repina, 2012) but is hard to identify from the ground-station in Ny Ålesund (south side of Kongsfjorden) given the rather low wind-speeds during this period. Winds that originate over land are likely colder, with lower humidity than marine air masses. Thus, the CMET observations of lower specific humidity between JD 131.40–131.5 (09:36–12:00 UTC) might be explained by fumigation from or simply sampling of such a channel outflow. Alternatively, the CMET's location over Kapp Mitra Penninsula at this time may indicate an even more local source of dry air impacting low levels. A final possibility could be overturning of air masses in the vertical, bringing less humid air, with higher potential temperature to lower altitudes. At mid-levels ($\sim$ 450 m) a relatively humid air layer persists, properties which suggest it likely has origins from the surface. It appears to be advected north-eastwards, potentially replenishing air over Svalbard to replace that which may be lost from the channel outflow. Further discussion is provided in conjunction with the WRF model results.

The CMET observations are compared to WRF model output at two time-periods, 07:00 and 15:00 UTC on 11 May (JD 131.3 and 131.6, respectively). Model output (in 2-D) is presented in two ways: (i) cross-sections of relative humidity (RH) and potential temperature with altitude along a transect in the WRF model (QNSE, YSU and MYJ schemes) that lies in an approximately S–N direction and is reasonably close to (but not identical to) the balloon flight path, see Fig. 8, (ii) maps of temperature and absolute humidity ($kg\,kg^{-1}$) at a constant model layer (equivalent to $\sim$ 300 m a.s.l. over the

ACPD
15, 27539–27573, 2015

oceans although reaching higher altitudes over the Svalbard terrain) that provide a geographic spatial context. For clarity, only output from WRF MYJ BL scheme is illustrated (see Supplement for QNSE and YSU schemes).

For (i), the WRF model temperature and humidity cross-sections at 07:00 and 15:00 UTC are shown alongside CMET observations along the whole balloon flight, in Figs. 9 and 10, respectively, and where the balloon locations at 07:00 and 15:00 UTC are denoted by a triangle or cross, respectively. The model generally agrees with the balloon observations: potential temperature increases with altitude, and surface temperature decreases with increasing latitude in the 07:00 UTC cross-section. Boundary layer height is denoted by a sharp humidity decrease, at approx. 600 m (declining to 400 m at higher latitudes) in the 07:00 UTC WRF cross-section. For all the model schemes, a greater relative humidity and a higher boundary layer is predicted in the 15:00 UTC cross-section, as expected from the diurnal cycle, whereby solar heating increases evaporation to enhance RH, and increases thermal buoyancy to enhance ABL height. By 15:00 UTC, the model potential temperature is also generally higher, however, surface temperatures now increases with latitude. This may reflect greater solar heating experienced at higher Arctic latitudes in the spring.

This overall RH trend of the model is in agreement to the observations: the CMET balloon data also exhibits a higher relative humidity at 15:00 UTC than 07:00 UTC. There is also some variability between the different model boundary layer schemes: for the 15:00 UTC cross-section boundary layer height, YSU > QNSE > MYJ in terms of both relative humidity and ABL height. However, diurnal variability is not the only control on ABL humidity (as discussed above). The geographical influence is illustrated by (ii); spatial maps of absolute humidity across a model layer (corresponding to ~ 300 m a.s.l. over oceans, somewhat higher over land) in Fig. 11. As expected, humidity in the marine air in the ice-free coastal region is greater than over Spitsbergen land, where temperatures were below freezing (see AWIPEV station time-series Fig. 4). Mixing or transfer between the marine- and land-influenced air masses can thus exert a significant influence on the observations, consistent with the findings from the CMET analysis

ACPD
15, 27539–27573, 2015

above. The model results presented at 07:00 UTC and 15:00 UTC clarify this influence in a geographic context. Between launch and 07:00 a.m. UTC the CMET moved into a more marine environment thus humidity increased. The balloon then moved northwards, perhaps drawn by a channel outflow from Kingsbay. Over this period humidity is constant or declining slightly, as the balloon passes across Kongsfjorden Bay and over the Kapp Mitra peninsula. From ~ midday to 15:00 UTC the humidity increases again as the balloon travels northwards (a temporary westerly diversion occurs following blocking of the low-level flow by Svalbard terrain). This humidity enhancement appears mostly caused by the diurnal effects of enhanced evaporation. Alternatively, simple transport of the balloon into or air-mass mixing with moister marine air could play a role, but in any case the diurnal humidity signal appears strong across this NW region. After 15:00 UTC the balloon was raised to higher altitudes hence the humidity decreased compared to that in the fixed model level (a similar decrease can be seen in the model altitude-transect plots, Fig. 10).

Finally, we return to the subject of the quasi-Lagrangian nature of the CMET balloon flight. A detailed analysis is beyond the scope of this study, nevertheless the wind, humidity and temperature observations indicate presence of more than one air mass in this coastal region. Whilst CMETs have previously been used in Lagrangian-type experiments to track the evolution of an airmass (e.g., Voss et al., 2010), this case-study presents more complex atmospheric conditions. Both vertical winds and horizontal wind-shear can affect the Lagrangian nature of the CMET balloon experiment. Vertical air mass movement is not measured by the CMET payload but is estimated by the WRF model to be sufficiently low (typically $\ll 0.01\,\mathrm{m\,s^{-1}}$) to be negligible in most cases, with the exception of localized areas in QNSE scheme (see Supplement, Fig. S4). The CMET balloon movement was itself used to determine horizontal winds (Fig. 7), and showed decoupled air flows of near opposite direction in the morning of 11 May (southerly winds at low altitudes, northerly winds at higher levels). Balloon soundings that traverse these layers will thus influence its overall trajectory. Trajectories were estimated from the observed winds at 50 m altitude intervals. This approximate tech-

ACPD
15, 27539–27573, 2015

nique assumes horizontally uniform flow (in the vicinity of the balloon and computed trajectories) during the 8 h period starting in the early morning of 11 May, Fig. 12. The lowermost layer exhibited greatest wind-speed thus has the longest (and least certain) trajectory, approximately double that of the balloon during the same period. The uppermost layer flows southwards before reversing direction, approximately returning to its initial position. The middle layer trajectory is quite similar to that of the CMET balloon, but is transported initially somewhat more westwards, and later somewhat more eastwards, due to the ESE winds experienced in the late morning (see Fig. 7). It is worth noting this final direction mirrors findings from two of the other CMET flights, whose initial paths out of Kongsfjorden deviated to the north-east into nearby Krossfjorden. While the balloon-based trajectories and repeating profile measurements are not Lagrangian, they do provide insight into the complex dynamics of low-altitude circulation influenced by complex terrain. Furthermore, the trajectories and profile data can be computed and displayed in near-real time, allowing future experiments to be modified during flight (e.g., to track specific layers or events). Such experiments can provide observational insights that help constrain the complex meteorology.

4 Conclusions

Five Controlled Meteorological (CMET) balloons were launched from Ny-Ålesund, Svalbard on 5–12 May 2011, to measure the meteorological conditions (RH, temperature, wind-speed) over Spitsbergen and in the surrounding Arctic region. Analysis of the meteorological data, in conjunction with simulations using the Weather and Research Forecasting (WRF) model at high (1 km) resolution provide insight into processes governing the Arctic atmospheric boundary layer and its evolution.

Three ABL parameterizations were investigated within the WRF model, YSU (Yonsei University), MYJ (Mellor–Yamada–Janjic) and QNSE (Quasi-Normal Scale Elimination). These schemes showed closer similarity to each other than between the model runs and the observations. This indicates more fundamental challenges to mesoscale

ACPD
15, 27539–27573, 2015

modelling in the Arctic, as identified from this study to include (i) the occurrence of inversions and low level jets over Svalbard topography in association with stable boundary conditions, which likely can only be captured at greater model resolution (ii) the presence of (fractional) sea-ice that acts to modify sea–air exchange, but whose dynamical representation in the model is not straight-forward to implement.

The WRF model simulations showed good general agreement to surface meteorological parameters (temperature, wind-speed, RH) in Ny Ålesund and Verlegenhuken, N Svalbard over 3–12 May 2011. However, temperatures were somewhat underestimated during colder periods, and surface winds were severely overestimated on 5–6 May in Ny Ålesund. Comparison of four CMET profiles over Svalbard topography to the WRF model indicated model difficulties in capturing inversion layers and a low-level jet (LLJ). The CMET observations thereby provided a context for the predicted high surface wind-speeds in Ny Ålesund, which were observed aloft but not at the surface during the campaign. A higher resolution is likely required to improve the model ability to simulate the small-scale atmospheric dynamics particularly for stable Arctic boundary layer conditions combined with Svalbard topography.

Two CMET soundings also probed the boundary layer over sea-ice to the east of Svalbard, during a balloon flight which despite good performance needed to be terminated to avoid encroaching on Russian territory. Model biases in wind-speed and surface level temperature (and inferred for specific humidity) over this region are likely due to the representation of sea-ice in the model. Whilst the ECMWF-derived sea-ice flag used appears reasonable, the presence of fractional sea-ice east of Svalbard may have enabled greater air–sea exchange of heat and moisture than predicted by the model, which assumed 100 % sea-ice coverage for positive sea-ice flag. Fractional representation of sea-ice in WRF is thus desirable, but is not straightforward to implement as sea-ice coverage depends on both sea-surface temperature driven freezing/melting processes and ocean-current driven advection, the latter being dominant East of Svalbard during spring. Improved sea-ice representation (e.g. applying a manual correction every 6 h) is recommended for future studies especially if multiple soundings over sea-

ACPD
15, 27539–27573, 2015

ice during longer duration CMET flights (i.e. northerly rather than easterly advected) can be achieved.

A series of continuous automated soundings was performed during a CMET flight over a sea-ice free region west of Svalbard, tracing atmospheric boundary layer temperature and relative humidity profiles along the flight and with altitude. Meteorological conditions encountered were complex, including a low-level flow decoupled from the air mass at higher altitudes. An increase in low-level relative humidity was observed, consistent with diurnal enhancement expected from evaporation. The WRF model predicted both an increase in RH and ABL height over the diurnal cycle concurrent with the CMET observations. The data-model interpretation also considers influence of air masses of different origin which augment the diurnal trends: air masses originating over the warm saline ocean waters have typically greater humidity than over the cold Svalbard topography.

Finally, the semi-Lagrangian nature of CMET flights is discussed. In this ABL study the balloon likely sampled different air masses through vertical soundings undertaken during the flight, under conditions of strong vertical wind-shear. Analysis of the observed wind-fields provides an indication of the balloon trajectory in the context of surrounding wind trajectories at different altitudes.

In summary, CMET balloons provide a novel technological means to profile the remote Arctic boundary layer over multi-day flights, including the capacity to perform multiple automated soundings. CMET capabilities are thus highly complementary to other Arctic observational strategies including fixed station, free and tethered balloons, and UAVs. Whilst UAVs offer full 3-D spatial control for obtaining the meteorological observations, their investigation zone is generally limited to tens of kilometers based on both range and regulatory restrictions. CMETs flights provide a relatively low-cost approach to observing the boundary layer at greater distances from the launch site (e.g. tens to hundreds of km), at altitudes potentially all the way down to the surface, and more remote from the disturbances of Svalbard topography. Analysis of the CMET observations along with output from a regional model output provides insights into the

ACPD
15, 27539–27573, 2015

processes that control the observed evolution of meteorological parameters and that pose a challenge to mesoscale simulations of the Arctic atmosphere.

The Supplement related to this article is available online at doi:10.5194/acpd-15-27539-2015-supplement.

Acknowledgements. This research was sponsored by the Research Council of Norway and the Svalbard Science Forum. We are very grateful to the joint French–German Arctic Research Base AWIPEV in Ny-Ålesund for logistical support, and Anniken C. Mentzoni for fieldwork assistance. T. J. Roberts acknowledges NSINK, an Arctic Field Grant, CRAICC, and the VOLTAIRE LABEX (VOLatils-Terre Atmosphère Interactions – Ressources et Environnement) ANR-10-LABX-100-01 (2011–2020) for funding. P. B. Voss acknowledges Smith College for support. This study occurred at the end of the Coordinated Investigation of the Climate–Cryosphere Interactions (CICCI) initiative.

References

Andreas, E. L., Claffey, K. J., and Makshtas, A. P.: Low-level atmospheric jets and inversions over the western Weddell sea, Bound.-Lay. Meteorol., 97, 459–486, 2000.

Andreas, E. L., Guest, P. S., Persson, P. O. G., Fairall, C. W., Horst, T. W., Moritz, R. E., and Semmer, S. R.: Near-surface water vapor over polar sea ice is always near ice saturation, J. Geophys. Res.-Oceans, 107, 8033, doi:10.1029/2000JC000411, 2002.

Bromwich, D. H., Hines, K. M., and Bai, L.-S.: Development and testing of polar weather research and forecasting model: 2. Arctic Ocean., J. Geophys. Res., 114, D08122, doi:10.1029/2008JD010300, 2009.

Chen, F. and Dudhia, J.: Coupling an advanced land-surface/hydrology model with the Penn State/NCAR MM5 modeling system. part i: Model description and implementation, Mon. Weather Rev., 129, 569–585, 2001.

Claremar, B., Obleitner, F., Reijmer, C., Pohjola, V., Waxeg, A., Karner, F., and Rutgersson, A.: Applying a mesoscale atmospheric model to Svalbard Glaciers, Adv. Meteorol., 2012, 321649, doi:10.1155/2012/321649, 2012.

ACPD
15, 27539–27573, 2015

Dudhia, J.: Numerical study of convection observed during the winter monsoon experiment using a mesoscale two-dimensional model, J. Atmos. Sci., 46, 3077–3107, 1989.
Esau, I. and Repina, I.: Wind climate in Kongsfjorden, Svalbard, and attribution of leading wind driving mechanisms through turbulence-resolving simulations, Adv. Meteorol., 2012, 568454, doi:10.1155/2012/568454, 2012.
Hines, K. M. and Bromwich, D. H.: Development and testing of polar weather research and forecasting (WRF) model. Part I: Greenland ice sheet meteorology, Mon. Weather Rev., 136, 1971–1989, 2008.
Hong, S.-Y., Dudhia, J., and Chen, S.-H.: A revised approach to ice microphysical processes for the bulk parameterization of clouds and precipitation, Mon. Weather Rev., 132, 103–120, 2004.
Hong, S.-Y., Noh, Y., and Dudhia, J.: A new vertical diffusion package with an explicit treatment of entrainment processes, Mon. Weather Rev., 134, 2318–2341, 2006.
Janjic, Z. I.: The step-mountain coordinate: physical package, Mon. Weather Rev., 118, 1429–1443, 1990.
Janjic, Z. I.: The Surface Layer Parameterization in the NCEP Eta Model, in: Research Activities in Atmospheric and Oceanic Modelling, CAS/C WGNE, 4.16–4.17, World Meteorological Organisation, Geneva, 1996.
Janjic, Z. I.: Nonsingular Implementation of the Mellor–Yamada Level 2.5 Scheme in the NCEP Meso Model, NCEP office note, 61 p., National Centre for Environmental Prediction, Camp Springs, Md., available at: http://www.emc.ncep.noaa.gov/officenotes/FullTOC.html#2000 (last access: 7 October 2015), 2002.
Kain, J. S.: The Kain–Fritsch convective parameterization: an update, J. Appl. Meteorol., 43, 170–181, 2004.
Kilpeläinen T., Vihma, T., and Olafsson, H.: Modelling of spatial variability and topographic effects over arctic fjords in svalbard, Tellus A, 63, 223–237, 2011.
Kilpeläinen T., Vihma, T., Manninen, M., Sjöblom A., Jakobson, E., Palo, T., and Maturilli, M.: Modelling the vertical structure of the atmospheric boundary layer over Arctic fjords in Svalbard, Q. J. Roy. Meteor. Soc., 138, 1867–1883, 2012.
Livik, G.: An observational and numerical study of local winds in kongsfjorden, Master Thesis at the University of Bergen, Spitsbergen, 2011.

ACPD
15, 27539–27573, 2015

Mäkiranta E., Vihma, T., Sjöblom A., and Tastula, E.-M.: Observations and modelling of the atmospheric boundary layer over sea-ice in a svalbard fjord, Bound.-Lay. Meteorol., 140, 105–123, 2011.

Mayer, S., Sandvik, A., Jonassen, M., and Reuder, J.: Atmospheric profiling with the UAS SUMO: a new perspective for the evaluation of fine-scale atmospheric models, Meteorol. Atmos. Phys., 116, 15–26, 2012a.

Mayer, S., Jonassen, M., Sandvik, A., and Reuder, J.: Profiling the arctic stable boundary layer in Advent Valley, Svalbard: measurements and simulations, Bound.-Lay. Meteorol., 143, 507–526, 2012b.

Mellor, G. L. and Yamada, T.: Development of a turbulence closure model for geophysical fluid problems, Rev. Geophys. Space Ge., 20, 851–875, 1982.

Mentzoni, A. C: Flexpart validation with the use of CMET balloons, Master Thesis at the University of Oslo, Oslo, 2011.

Mlawer, E. J., Taubman, S. J., Brown, P. D., Iacono, M. J., and Clough, S. A.: Radiative transfer for inhomogeneous atmospheres: Rrtm, a validated correlated-k model for the longwave, J. Geophys. Res., 102, 16663–16682, 1997.

Mölders N., and Kramm, G.: A case study on wintertime inversions in interior Alaska with WRF, Atmos. Res., 95, 314–332, 2010.

Persson, P. O. G., Fairall, C. W., Andreas, E. L., Guest, P. S., and Perovich, D. K.: Measurements near the atmospheric surface flux group tower at sheba: near-surface conditions and surface energy budget, J. Geophys. Res., 107, 8045–8079, 2002.

Riddle, E. E., Voss, P. B., Stohl, A., Holcomb, D., Maczka, D., Washburn, K., and Talbot, R. W.: Trajectory model validation using newly developed altitude-controlled balloons during the international consortium for atmospheric research on transport and transformations 2004 campaign, J. Geophys. Res., 111, D23S57, doi:10.1029/2006JD007456, 2006.

Rinke, A., Dethloff, K., Cassano, J., Christensen, J., Curry, J., Du, P., Girard, E., Haugen, J.-E., Jacob, D., Jones, C., Kltzow, M., Laprise, R., Lynch, A., Pfeifer, S., Serreze, M., Shaw, M., Tjernstrm, M., Wyser, K., and Agar, M.: Evaluation of an ensemble of Arctic regional climate models: spatiotemporal fields during the sheba year, Clim. Dynam., 26, 459–472, 2006.

Skamarock, W., Klemp, J., Dudhia, J., Gill, D., Barker, D., Duda, M. H. X. Y., and Wang, W.: A description of the advanced research WRF version 3, NCAR Tech. Note NCAR/TN-4751+STR, 125 p., available at: www2.mmm.ucar.edu/wrf/users/docs/arw_v3.pdf (last access: 7 October 2015), 2008.

ACPD
15, 27539–27573, 2015

Stenmark, A., Hole, L. R., Voss, P., Reuder, J., and Jonassen, M. O.: The influence of nunataks on atmospheric boundary layer convection during summer in Dronning Maud Land, Antarctica, J. Geophys. Res. Atmos., 119, 6537–6548, doi:10.1002/2013JD021287, 2014.

Stohl, A., Wotawa, G., Seibert, P., and Kromp-Kolb, H.: Interpolation errors in wind fields as a function of spatial and temporal resolution and their impact on different types of kinematic trajectories, J. Appl. Meteorol., 34, 2149–2165, 1995.

Stohl, A., Hittenberger, M., and Wotawa, G.: Validation of the lagrangian particle dispersion model flexpart against large-scale tracer experiment data, Atmos. Environ., 32, 4245–4264, 1998.

Sukoriansky, S., Galperin, B., and Perov, V.: A quasi-normal scale elimination model of turbulence and its application to stably stratified flows, Nonlin. Processes Geophys., 13, 9–22, doi:10.5194/npg-13-9-2006, 2006.

Vihma, T., Pirazzini, R., Fer, I., Renfrew, I. A., Sedlar, J., Tjernström, M., Lüpkes, C., Nygård, T., Notz, D., Weiss, J., Marsan, D., Cheng, B., Birnbaum, G., Gerland, S., Chechin, D., and Gascard, J. C.: Advances in understanding and parameterization of small-scale physical processes in the marine Arctic climate system: a review, Atmos. Chem. Phys., 14, 9403–9450, doi:10.5194/acp-14-9403-2014, 2014.

Voss, P. B., Zaveri, R. A., Flocke, F. M., Mao, H., Hartley, T. P., DeAmicis, P., Deonandan, I., Contreras-Jiménez, G., Martínez-Antonio, O., Figueroa Estrada, M., Greenberg, D., Campos, T. L., Weinheimer, A. J., Knapp, D. J., Montzka, D. D., Crounse, J. D., Wennberg, P. O., Apel, E., Madronich, S., and de Foy, B.: Long-range pollution transport during the MILAGRO-2006 campaign: a case study of a major Mexico City outflow event using free-floating altitude-controlled balloons, Atmos. Chem. Phys., 10, 7137–7159, doi:10.5194/acp-10-7137-2010, 2010.

Voss, P. B., Hole, L. R., Helbling, E., and Roberts, T. J.: Continuous in-situ soundings in the Arctic boundary layer: a new atmospheric measurement technique using controlled meteorological balloons, J. Intell. Robot. Syst., 70, 609–617, 2013.

ACPD
15, 27539–27573, 2015

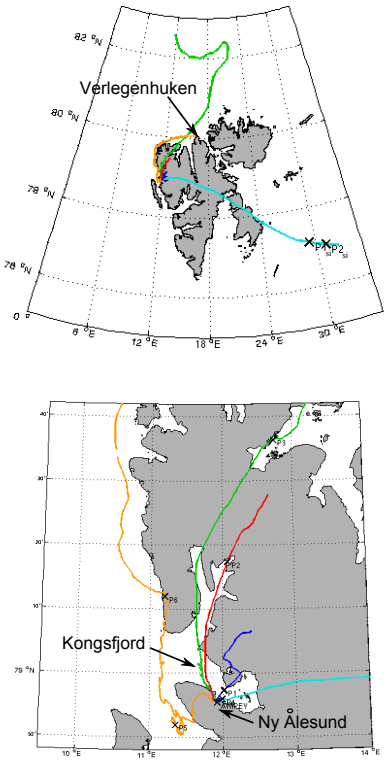

Figure 1. Trajectories of five CMET balloons launched from Ny-Ålesund in May 2011. Soundings used for comparison to WRF are labelled P1si, P2si (over sea-ice east of Svalbard for comparison to WRF model run 2), and P1, P2, P3, P4 (over Svalbard topography for comparison to WRF model run 1). P5 and P6 denote balloon locations at 03:00 and 12:00 UTC during flight 5 whilst the balloon made automated continuous soundings to the west of Svalbard.

ACPD
15, 27539–27573, 2015

CMET balloon profiling of Arctic ABL

T. J. Roberts et al.

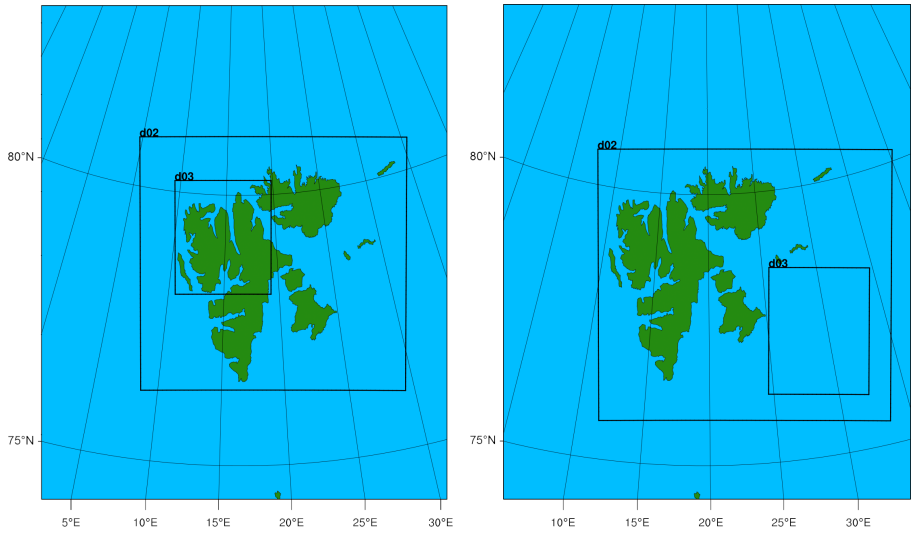

Figure 2. Nested grids of the WRF model setup for the two model runs.

ACPD
15, 27539–27573, 2015

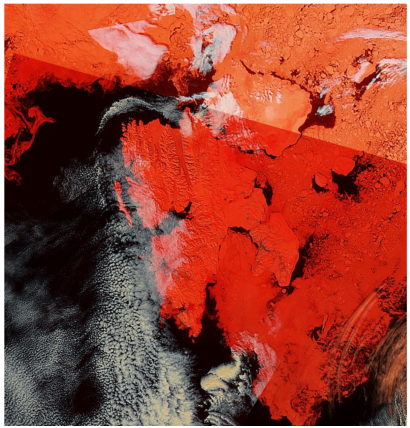

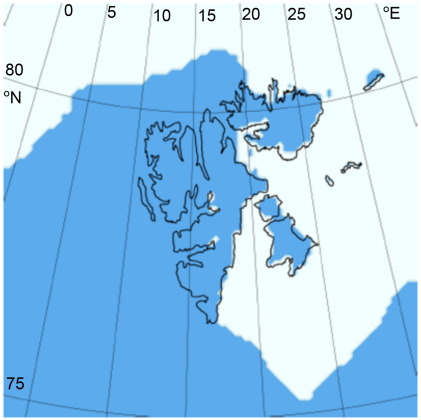

Figure 3. Comparison of sea-ice conditions around Svalbard (left) to sea-ice flag in WRF model (right). Lance rapid response image from the MODIS satellite (downloaded from http://lance-modis.eosdis.nasa.gov/, land and sea-ice are shown in red, cloud cover in white) for 5 May 2011 and the ECMWF sea-ice flag as used in the WRF model (white = 1, blue = 0).

ACPD
15, 27539–27573, 2015

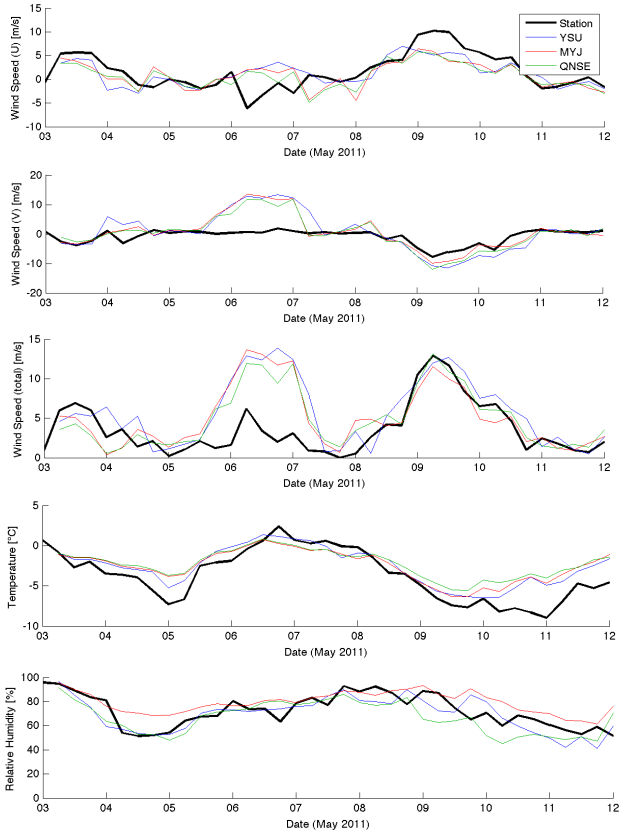

Figure 4. 6 hourly averaged meteorology time-series from the Ny-Ålesund AWIPEV station compared to WRF model simulation with 3 boundary layer schemes (YSU, MYJ, QNSE).

ACPD
15, 27539–27573, 2015

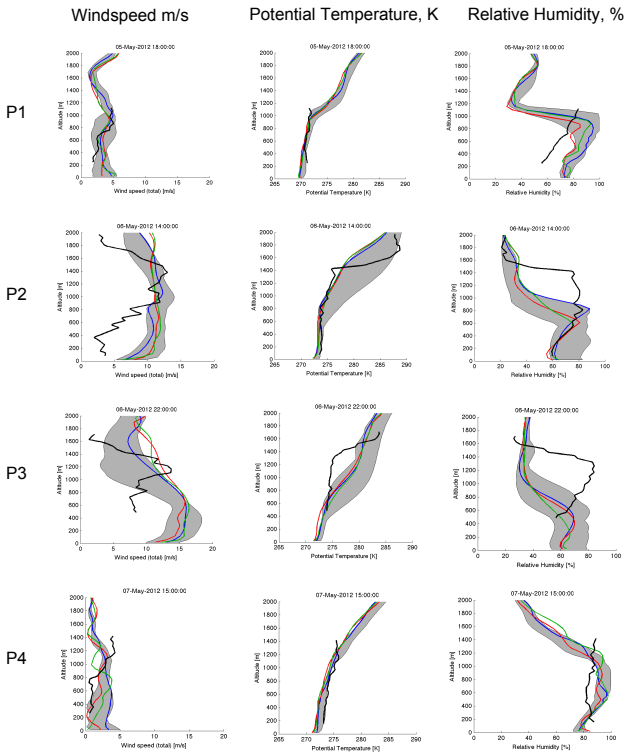

Figure 5. CMET wind-speed, potential temperature and relative humidity profiles P1–P4 made over Svalbard topography compared to WRF model. The 3 ABL schemes are depicted with the same colour key as for Fig. 4. The grey band represents a range of 25 profiles of the YSU scheme on a 4 km × 4 km square centred the balloon profile to illustrate horizontal variability in the model output.

ACPD
15, 27539–27573, 2015

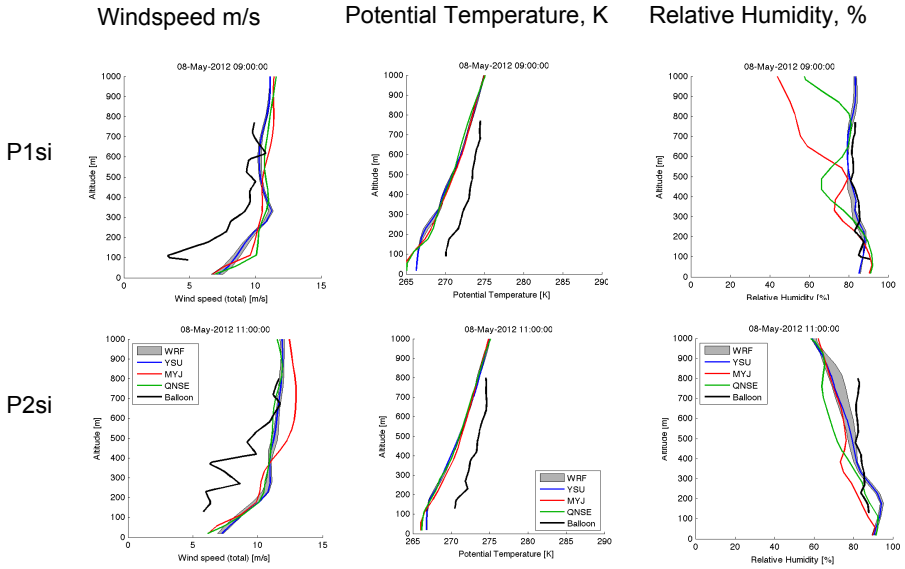

Figure 6. As for Fig. 5 but for profiles P1si and P2si over sea-ice east of Svalbard.

ACPD
15, 27539–27573, 2015

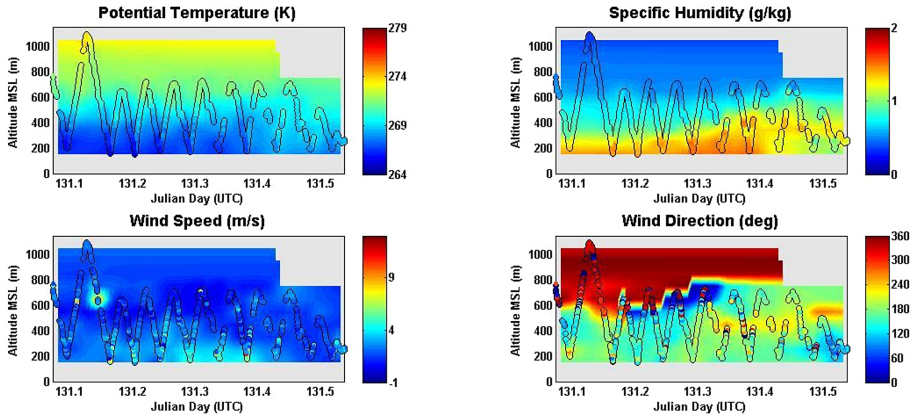

Figure 7. Potential temperature, specific humidity, wind-speed and wind direction determined from the CMET balloon observations (131.08 to 131.52 JD, equivalent to ~ 02:00 to 12:30 UTC on 11 May) of flight 5 during a series of automated soundings between 150 and 700 m altitude. Data between the balloon soundings has been interpolated to facilitate visualization.

ACPD
15, 27539–27573, 2015

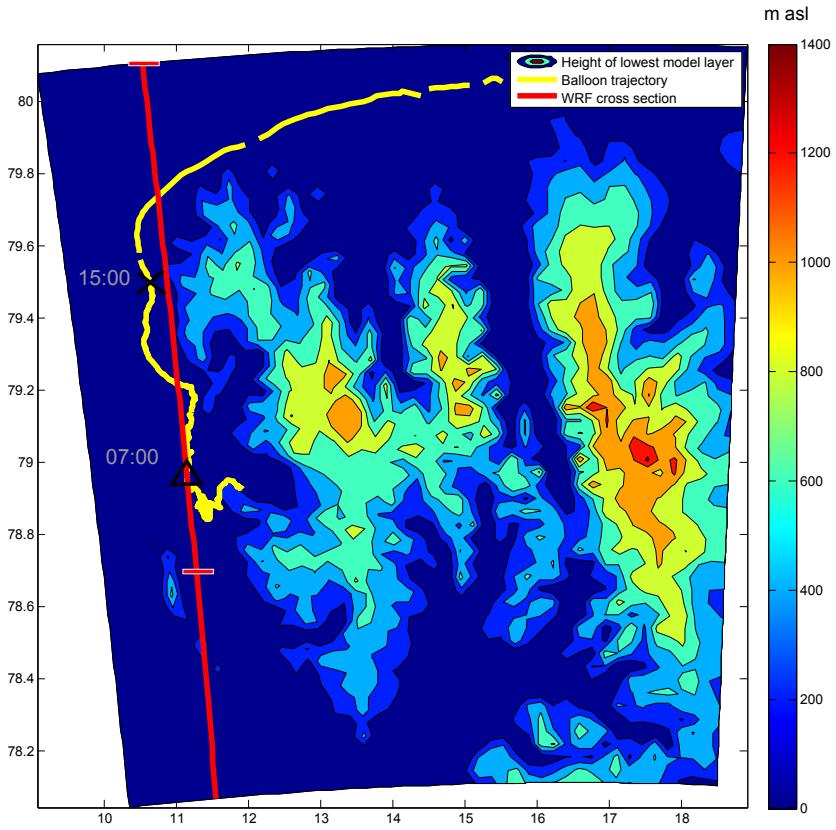

Figure 8. Map of the WRF cross-section transect (red lines) and the CMET balloon trajectory (yellow line) of flight 5. Approximate balloon locations at 07:00 and 15:00 UTC (JD 131.3 and 131.6) are denoted by a triangle and cross, respectively.

ACPD
15, 27539–27573, 2015

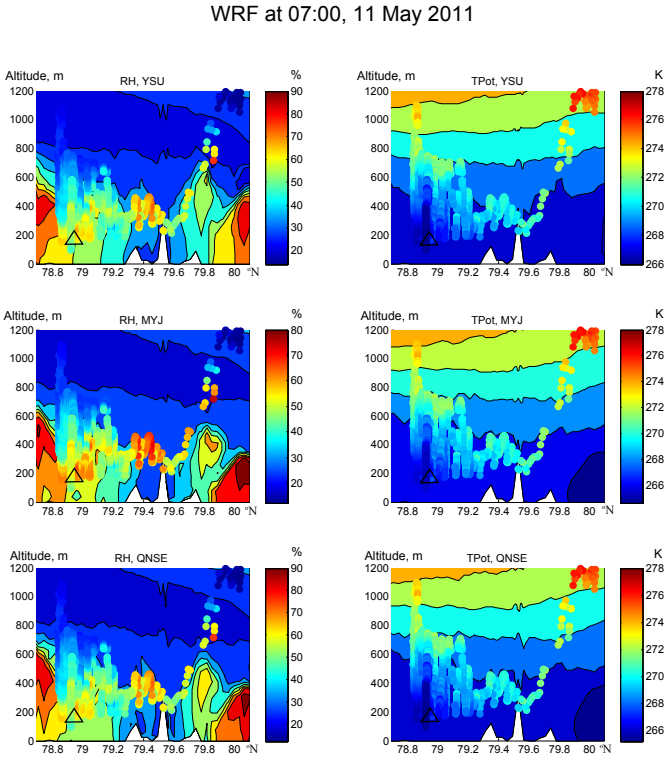

Figure 9. Crossection of the WRF model relative humidity (RH) and potential temperature (TPot) at 07:00 UTC (JD 131.3) shown as a function of altitude along the transect line. CMET observations for the whole flight are also illustrated, with approximate balloon location at 07:00 UTC denoted by a triangle.

ACPD
15, 27539–27573, 2015

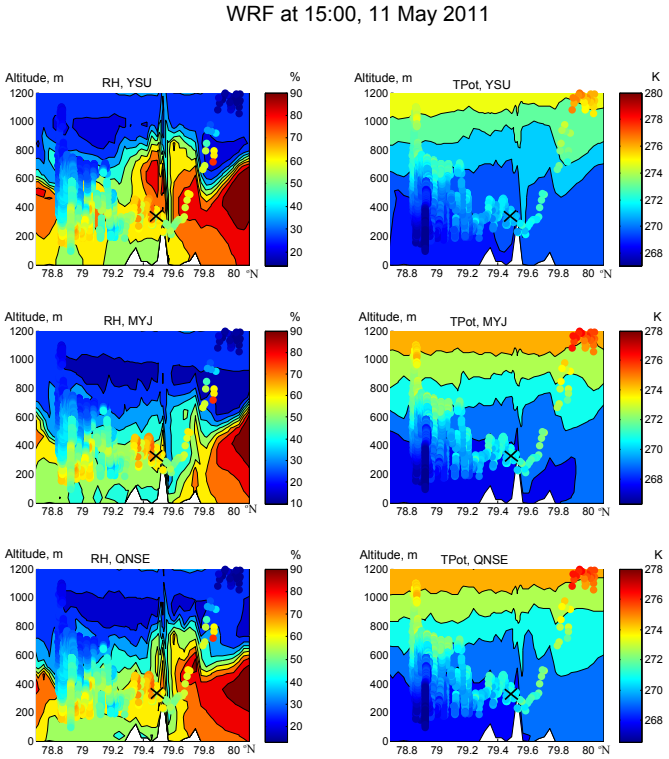

Figure 10. Crossection of the WRF model relative humidity (RH) and potential temperature (TPot) at 15:00 UTC (JD 131.6) shown as a function of altitude along the transect line. CMET observations for the whole flight are also illustrated, with approximate balloon location at 15:00 denoted by a cross.

ACPD
15, 27539–27573, 2015

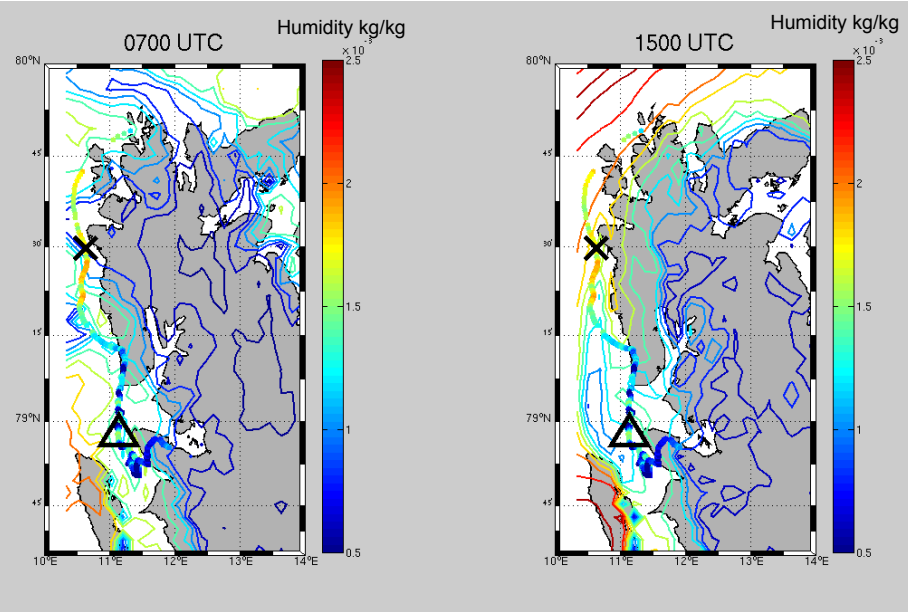

Figure 11. Absolute humidity (kg kg^{-1}) in the WRF model (with MYJ scheme) layer corresponding to 300 m a.s.l. (over oceans) at 07:00 and 15:00 UTC compared to the CMET flight 5 whilst it performed automated ABL soundings centred around ~ 300 m a.s.l. The CMET balloon positions at 07:00 and 15:00 UTC (equivalent to JD 131.3 and JD 131.6) are marked by a triangle and a cross, respectively. Data from the final stages of the balloon flight (at greater than ~ 1000 m a.s.l. thus not probing the ABL) has been omitted for clarity.

ACPD
15, 27539–27573, 2015

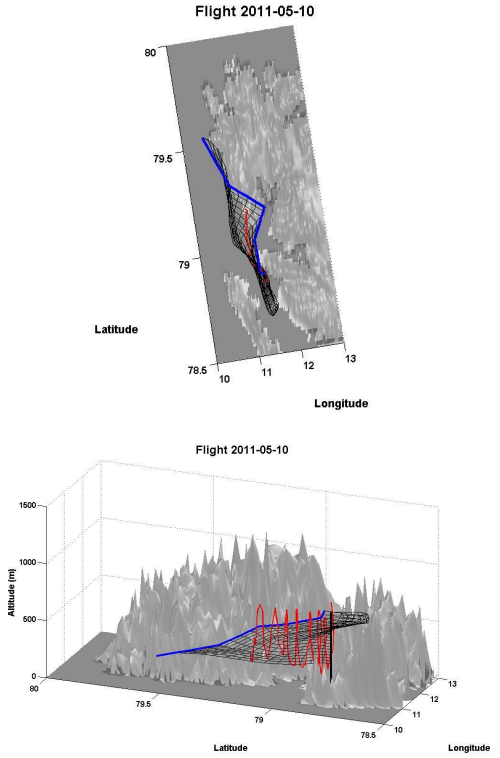

Figure 12. Approximate air-parcel trajectories calculated from the CMET balloon-measured winds. The trajectories are calculated over an eight hour period for each 50 m altitude layer. The red line shows the actual balloon track, the black vertical line shows the initialization, the black grid shows the trajectories, and blue line shows the final location after eight hours.

ACPD
15, 27539–27573, 2015